

Understanding Quantum Advantage using Parameterized Quantum Circuit Learning for Quantum Chemical Applications

Grier M. Jones,^{†,‡} Nick Taylor,[†] Viki Kumar Prasad,^{†,‡} Ulrich Fekl,^{*,‡} and
Hans-Arno Jacobsen^{*,†}

[†] *The Edward S. Rogers Sr. Department of Electrical and Computer Engineering, University of
Toronto, 10 Kings College Road, Toronto, Ontario, Canada M5S 3G4*

[‡] *Department of Chemical and Physical Sciences, University of Toronto Mississauga, 3359
Mississauga Road, Mississauga, Ontario, Canada L5L 1C6*

E-mail: ulrich.fekl@utoronto.ca; jacobsen@eecg.toronto.edu

Abstract

Within the quantum machine learning (QML) field, parameterized quantum circuits (PQCs), built using fixed and parameterized gates, offer a hybrid approach for complex machine learning tasks. While many potential use cases have been proposed, the exploration of relevant datasets for chemists is lacking. Our study seeks to understand the possible advantages and disadvantages of PQCs for two chemically relevant datasets: one based on the bond separation energies of 49 different classes of bonds, called the BSE49 dataset, and another consisting of water confirmations, where coupled-cluster singles and doubles (CCSD) wave functions are predicted using electronic structure theory data from lower-level methods using the data-driven coupled-cluster (DDCC) method. In our study, we examine a combinatorial space of 14 data encoding layers and 12 variational (ansatz) layers,

for a combined total of 168 PQCs. To calibrate our PQCs, we utilize a dataset of noisy linear, quadratic, and sine functions to explore the effects of the circuit width and depth, the effects of the feature set size, and various error mitigation techniques. Following this step, we similarly examine our chemically relevant datasets. Our work highlights the difficulties in encoding classical molecular representations in a PQC for predicting bond separation energies and the aptitude for PQCs for predicting molecular wave functions.

1 Introduction

In recent years, machine learning (ML) has emerged as a popular tool in chemistry for revealing new patterns in data, providing new insights beyond simple models and human experience, accelerating computations, and analyzing chemical space. For computational chemists, the primary goal of applying ML is often to bypass the explicit calculation of molecular properties, which can be computationally expensive for large datasets.¹ ML can be applied to a diverse set of applications including, but not limited to, accelerating molecular simulations,^{2–4} determining molecular properties,^{5–9} and for discovering new catalysts,^{10–12} drugs,^{13,14} and materials.^{15–17} Since these applications can become resource intensive, regarding the generation of training data using traditional computational chemistry approaches and the training of large-scale ML models, computational chemistry and ML practitioners have explored new acceleration platforms, such as graphical processing units (GPUs) and tensor processing units (TPUs).^{3,13,18–22}

Alternatively, computational approaches incorporating the quantum mechanical principles of superposition and entanglement, called quantum computing (QC), have become increasingly popular for chemical applications due to possible quantum speedups for quantum chemical calculations.²³ For computational chemistry, methods such as the quantum phase estimation (QPE)^{24–29} algorithm have been shown to offer exponential speedups over classical methods. Despite the promising speedups, QPE requires long coherence times, while the current generation of quantum processing units (QPUs), are often too noisy for practical applications. Alternatively, methods

based on the variational principle, such as the variational quantum eigensolver (VQE),^{30–33} have been proposed as a quantum-classical hybrid approach, capable of running on noisy, near-term quantum devices.

While most QC studies that are relevant to computational chemists focus on creating more efficient electronic structure methods on quantum computers,^{23,34–36} an approach that combines both ML and QC, is quantum machine learning (QML). Using either formal mathematical proofs or numerical results based on empirical observations, QML has shown potential quantum speedups for various applications using a diverse set of implementations.³⁷ While several classes of QML algorithms have shown promise for providing flexible ML models, parameterized quantum circuits (PQCs) are capable of achieving non-trivial results on near-term quantum hardware. PQCs formulate the ML algorithm as a variational problem optimized using a hybrid approach using both classical and quantum hardware.³⁸ Like classical ML approaches, PQCs have been applied for several chemistry use cases such as drug^{39–45} and materials discovery,^{46–48} the prediction of proton affinities,⁴⁹ and experimental molecular properties, including the log solubility in water, melting point, octanol/water distribution coefficient, and hydration free energy of small molecules in water.⁵⁰ Despite the broad range of topics covered in these studies and the interest among computational chemists in exploring PQCs for chemical applications, studies analyzing the potential benefits or drawbacks of using QML for quantum chemistry are lacking.

In this study, we address this by analyzing a diverse set of PQCs using two datasets related to computational chemistry. The first dataset, BSE49 consists of bond separation energies (BSEs) of 49 unique bond types, calculated using the highly accurate (RO)CBS-QB3 composite method.⁵¹ The second dataset consists of water conformers calculated with coupled-cluster singles and doubles (CCSD) using the data-driven coupled-cluster (DDCC) scheme of Townsend and Vogiatzis.^{52,53} Both datasets offer a unique perspective on the aptitude of applying PQCs on classical and quantum data⁵⁴ since the models based on BSE49 rely on classical molecular representations,⁵⁵ such as Molecular ACCess Systems (MACCS)⁵⁶ or Morgan fingerprints,^{57,58} as input, while the input features in the DDCC method encode explicit quantum information related

to the molecular electronic structure. In this study, we introduce *qgress* a modular Python framework, based on PennyLane⁵⁹ and Qiskit,⁶⁰ for exploring PQCs for regression-based QML tasks. To this end, we explore the effects of classical and quantum data using a broad set of 168 unique PQCs, based on a combination of 14 data encoding and 12 variational layers. We then perform an analysis of circuit depth on model performance, using two different expansion strategies, one based on data re-uploading⁶¹ and the other based on increasing the number of model parameters using additional variational layers. Using these insights, we then analyze how the best model performs using fake and real Qiskit backends. Lastly, we provide a detailed discussion on the efficiency and performance of PQCs, with insights to what quantum advantage could mean with respect to classical ML models.

2 Methods

PQCs typically consist of three components: encoding layers that map features onto a quantum circuit, variational layers with classically optimized parameters, and measurement layers that provide numerical estimates of the regression target values.³⁹ Choosing the optimal encoding layer can be a challenging task due to costs associated with mapping the input data to qubits.³⁷ Due to this fact, we choose existing encoding layers that have shown promising results for regression tasks such as Mitarai (M),⁶² single- (A1) and double-angle (A2) encoding layers found in Ref.³⁹, along with the instantaneous quantum polynomial (IQP) circuit found in Refs.⁶³ and⁶⁴.

To maintain a general notation, in the following section we follow the notations derived from Ref.³⁹. Encoding layers work by mapping a given d -dimensional feature vector, $\mathbf{x} = (x_1, x_2, \dots, x_d)^T \in \mathbb{R}^d$, normalized on the range $[-1, 1]$, onto a quantum circuit using a unitary matrix, denoted as $U_{\Phi(\mathbf{x})}$, to produce the quantum state $U_{\Phi(\mathbf{x})}|0\rangle^{\otimes n}$, where n are the number of qubits. More generally, the encoding layer can also incorporate both unitary and entanglement gates, such that

$$U_{\Phi(x)} = \prod_l E_{\text{ent}}^l U_{\phi_l(\mathbf{x})}, \quad (1)$$

where, E_{ent}^l denotes the entangling gates, e.g., CNOT or CZ, and $U_{\phi_l(\mathbf{x})}$ denotes the choice of encoding unitaries.

In this study, like in Ref.³⁹, we explore encoders with $l = 1, 2$. When $l = 1$, this forms the simplest encoding layers with E_{ent}^1 being absent, e.g. corresponding to the identity (**I**). Using the previously defined general notation, the simplest encoding layer, single-angle encoding (Fig. 1 **(a)**), is then defined as,

$$U_{A1} = \prod_{i=0}^n R_i^Y(x_i), \quad (2)$$

where R_i^Y denotes a parameterized Y rotation gate on qubit i . Single-angle encoding, or qubit encoding, is structured similarly to a product of unentangled quantum states and have a similar mathematical structure as a product of local kernels where each x_i is encoded in a local feature map.^{38,65}

The next encoder, double-angle encoding (Fig. 1 **(b)**) utilizes a parameterized Y rotation gate on qubit i , similar to $A1$, with the addition of a parameterized Z rotation gate on qubit i , denoted as

$$U_{A2} = \prod_{i=0}^n R_i^Z(x_i)R_i^Y(x_i), \quad (3)$$

which introduces additional redundancy by encoding two angles on the Bloch sphere. An extension of the double-angle encoding is the Mitarai encoding layer (Fig. 1 **(c)**), which includes an arccosine function on the parameterized Z gate and arcsine on the parameterized Y gate,

$$U_M = \prod_{i=0}^n R_i^Z(\arccos(x_i^2))R_i^Y(\arcsin(x_i^2)). \quad (4)$$

This unitary is physically motivated by expanding a density operator in terms of a set of Pauli operators, as highlighted in Ref.⁶²

The last and most complex encoding layer is the instantaneous quantum polynomial (IQP) (Fig.

1 (d)) proposed by Havlicek *et al.*,⁶⁴

$$U_{\text{IQP}} = \prod_{i=0}^n H_i R_i^Z(x_i) \prod_{i < j} ZZ_{ij}, \quad (5)$$

where H_i denotes a Hadamard gate on qubit i and ZZ_{ij} denotes a two-qubit entangling gate defined as $ZZ_{ij} = e^{-ix_i x_j \sigma_z \otimes \sigma_z}$. It should be noted that under specific complexity and theoretic assumptions, IQP circuits cannot be efficiently simulated using classical resources and therefore offer a circuit that can only be simulated efficiently using quantum resources.^{66,67}

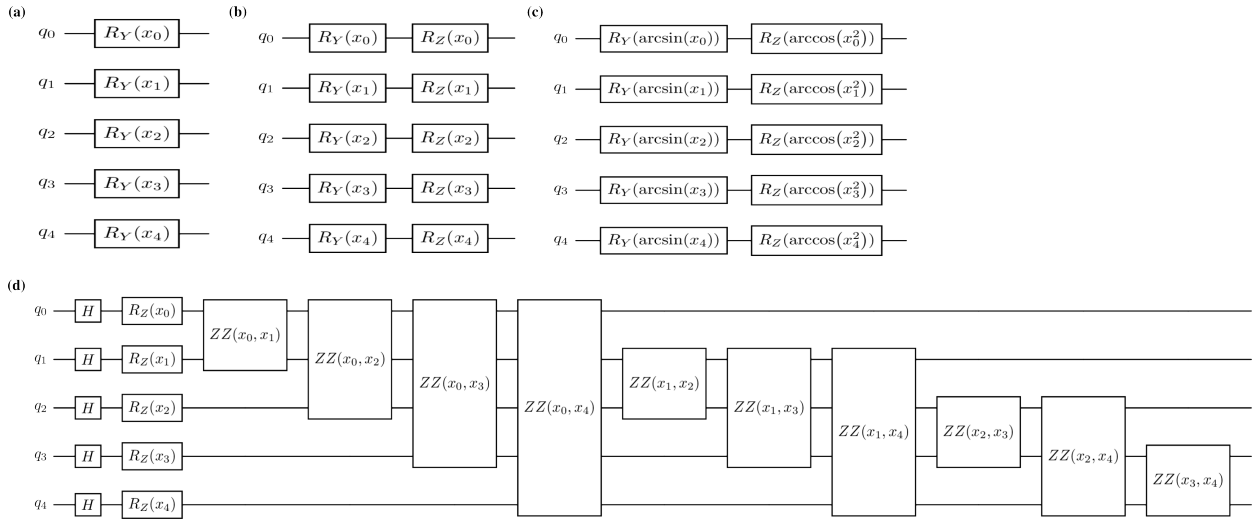


Figure 1: Five qubit examples of the (a) single angle (A1), (b) double angle (A2), (c) Mitarai (M), and (d) Instantaneous Quantum Polynomial (IQP) encoders used in this study.

When $l = 2$, more complex circuits can be generated, like in Ref.³⁹, where we choose the entanglement gates, E_{ent}^1 and E_{ent}^2 , to be equivalent and the encoding layer takes the following form, $U_{\Phi(\mathbf{x})} = E_{\text{ent}} U_{\phi_2(\mathbf{x})} E_{\text{ent}} U_{\phi_1(\mathbf{x})}$. Additionally, we exclude IQP encoding when $l = 2$ due to the increased computational costs associated with the circuit depth when compared to the expanded models based on A1, A2, and M encoding. Therefore, when we exclude IQP, there are five unique combinations of $U_{\phi_1(\mathbf{x})}$ and $U_{\phi_2(\mathbf{x})}$ (M-M, A1-A1, A2-A2, M-A1, and M-A2) and two different entanglement layer options (CNOT and CZ) for a total of 10 encoding circuits with $l = 2$. The common notation for these circuits is $U_{\phi_1(\mathbf{x})} - U_{\phi_2(\mathbf{x})} - E_{\text{ent}}$ where two example encoding circuits are

M–M–CNOT and M–A1–CNOT. The 14 encoding circuits used throughout this study are shown in Table 1, where the first column shows the label, second column the first unitary ($U_{\phi_1(\mathbf{x})}$), third column the second unitary ($U_{\phi_2(\mathbf{x})}$), and last column the entanglement gates (E_{ent}).

Table 1: The 14 encoding layers used in this study where the first column shows the encoding circuit name, second column the unitary for $l = 1$, third column the unitary for $l = 2$, and last column the corresponding entanglement gates.

Name	$U_{\phi_1(\mathbf{x})}$	$U_{\phi_2(\mathbf{x})}$	E_{ent}
A1	U_{A1}	—	—
A2	U_{A2}	—	—
M	U_{M}	—	—
IQP	U_{IQP}	—	—
A1–A1–CNOT	U_{A1}	U_{A1}	E_{CNOT}
A2–A2–CNOT	U_{A2}	U_{A2}	E_{CNOT}
M–M–CNOT	U_{M}	U_{M}	E_{CNOT}
M–A1–CNOT	U_{M}	U_{A1}	E_{CNOT}
M–A2–CNOT	U_{M}	U_{A2}	E_{CNOT}
A1–A1–CZ	U_{A1}	U_{A1}	E_{CZ}
A2–A2–CZ	U_{A2}	U_{A2}	E_{CZ}
M–M–CZ	U_{M}	U_{M}	E_{CZ}
M–A1–CZ	U_{M}	U_{A1}	E_{CZ}
M–A2–CZ	U_{M}	U_{A2}	E_{CZ}

The next layer in a PQC that follow the encoding layer, are the variational layers. The variational layers introduce trainable parameters, that can be optimized using classical compute resources, into the quantum circuit and provide flexibility to the QML models. These layers have a general form, defined as,

$$U(\boldsymbol{\theta}) = \prod_v U_v(\boldsymbol{\theta}_v), \quad (6)$$

where $\boldsymbol{\theta}$ denote the variational parameters, v denote the number of times that the layer is repeated within the circuit, and all entanglement gates are implicitly included in $U_v(\boldsymbol{\theta}_v)$. In our study, we examine 12 variational circuits, found in,⁶⁸ as shown in Fig. 2. The unique names of the 12 variational circuits are as follows: Modified-Pauli-CRZ (Fig. 2(a)), Modified-Pauli-CRX (Fig. 2(b)), Efficient-CRZ (Fig. 2(c)), Efficient-CRX (Fig. 2(d)), HWE-CNOT (Fig. 2(e)), HWE-CZ (Fig. 2(f)), ESU2 (Fig. 2(g)), Full-Pauli-CRZ (Fig. 2(h)), Full-Pauli-CRX (Fig. 2(i)), Hadamard

(Fig. 2(j)), Full-CRZ (Fig. 2(k)), and Full-CRX (Fig. 2(l)).

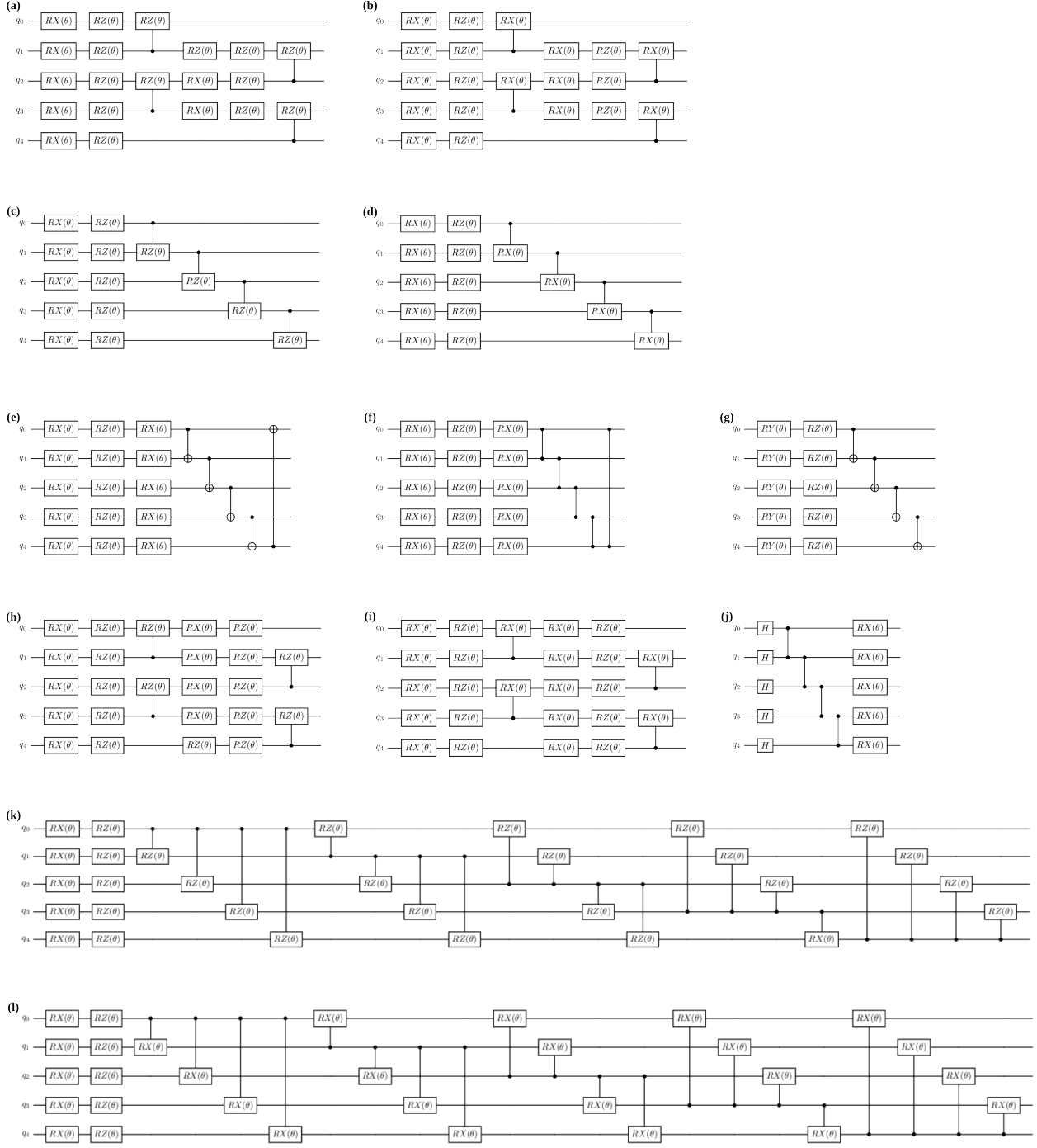


Figure 2: The 12 variational circuits include (a) Modified-Pauli-CRZ, (b) Modified-Pauli-CRX, (c) Efficient-CRZ, (d) Efficient-CRX, (e) HWE-CNOT, (f) HWE-CZ, (g) ESU2, (h) Full-Pauli-CRZ, (i) Full-Pauli-CRX, (j) Hadamard, (k) Full-CRZ, and (l) Full-CRX

To introduce more model parameters and increase the expressibility and nonlinearity of the

PQCs, two expansion strategies can be explored. The first we denoted as the number of ansatz layers (AL), where v can be increased to introduce more unique trainable parameters into the PQC. The second expansion strategy builds on the work of Pérez-Salinas *et al.* that showed data re-uploading in PQCs is equivalent to the Universal Approximation Theorem for artificial neural networks.⁶¹ This is achieved combining Eqs. 1 and 6 into a general circuit,

$$|\Psi\rangle = U(\boldsymbol{\theta})U_{\Phi(\mathbf{x})}|0\rangle^{\otimes n} = \prod_k \left(\prod_v U_v(\boldsymbol{\theta}_v) \prod_l E_{\text{ent}}^l U_{\phi_l(\mathbf{x})} \right) |0\rangle^{\otimes n}, \quad (7)$$

where k denotes the re-upload depth (RUD) of the circuit.

The last component of a PQC is measurement, which is required to recover the predicted target values, \hat{y}_i , of the machine learning model that are used to update the model parameters. This is performed by measuring the quantum state, $|\Psi\rangle$, using the Pauli Z operator on the first qubit denoted as,

$$\hat{y}_i = \langle \Psi | Z_0 | \Psi \rangle_i, \quad (8)$$

and passing the set of predicted target values, $\hat{\mathbf{y}} = (\hat{y}_1, \dots, \hat{y}_N) \in \mathbb{R}^N$, where N is the number of samples, to the loss function, $\mathcal{L}(\mathbf{y}, \hat{\mathbf{y}})$, where y_i belongs to the set of true target values $\mathbf{y} = (y_1, \dots, y_N) \in \mathbb{R}^N$. While \mathcal{L} can be any loss function relevant for regression-based ML tasks, we choose to mean square error to be the loss function,

$$\mathcal{L}(\mathbf{y}, \hat{\mathbf{y}}) = \frac{1}{N} \sum_{i=1}^N (y_i - \hat{y}_i)^2. \quad (9)$$

Implementation

To facilitate the exploration of the large design space of the PQCs, we created a modular Python-based workflow called *qregress*. *qregress* incorporates circuits generated using both PennyLane⁵⁹ and Qiskit,⁶⁰ along with state-vector simulation using Qulacs,⁶⁹ noisy simulation using *qiskit-aer* with the *FakeQuebec* backend backend as implemented in Qiskit,⁶⁰ and real using *ibm_quebec*. All state-vector simulations are performed using the PennyLane code base, while all calculations

using *FakeQuebec* and *ibm_quebec* are ran using Qiskit due to the PennyLane-Qiskit plugin not including Batch execution modes. Additionally, state-vector simulations use the PennyLane implementation of the Simultaneous Perturbation Stochastic Approximation method (SPSA), while for the experiments run using *FakeQuebec* and *ibm_quebec* utilizes the Constrained Optimization By Linear Approximation (COBYLA) optimizer, as implemented ing SciPy.⁷⁰

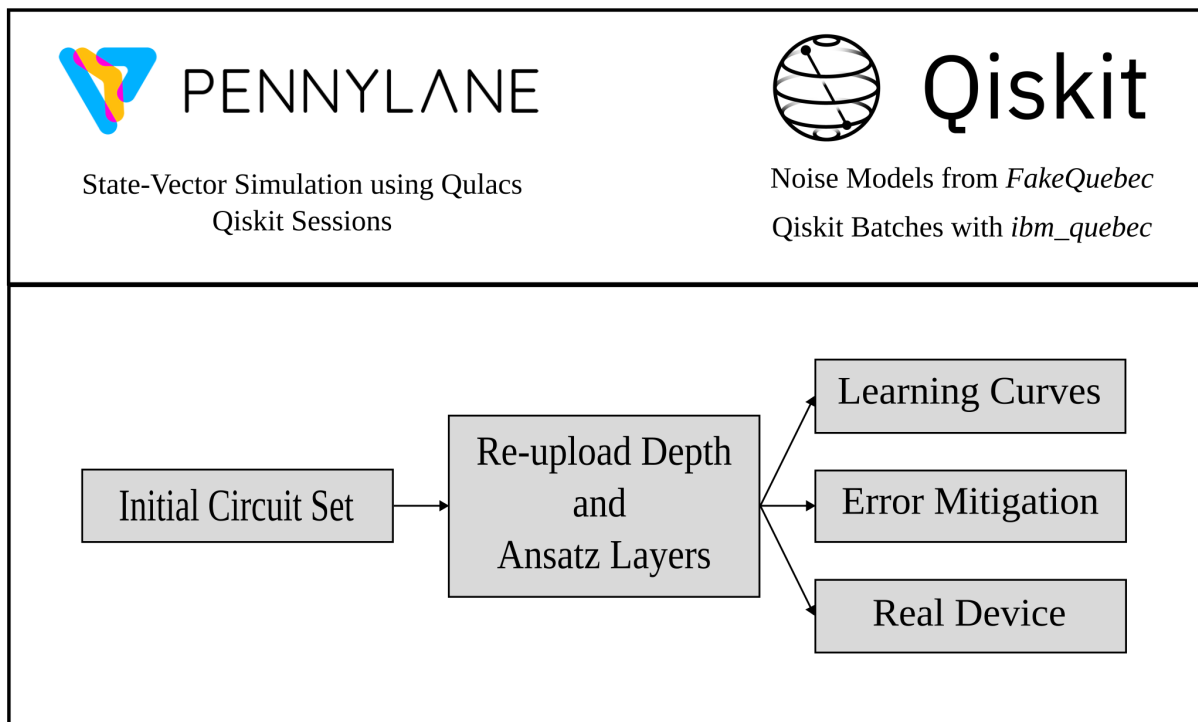


Figure 3: REMAKE to include cool code pic. Make this figure highlight the modularity of *qregress*

Each optimizer was chosen based on the performance for the given task. All features (\mathbf{x}) and target values (y) were scaled using the MinMaxScaler in Scikit-learn,⁷¹ such that all features and target values are $\mathbb{R} \in [-1, 1]$. For the simulations using *FakeQuebec* and experiments on *ibm_quebec* we utilize Twirled Readout Error eXtinction (TREX) error mitigation.

Used QisKit for real and fake back end using Qiskit Batches

optimization levels none (0)

“No optimization: typically used for hardware characterization Basic translation and Layout/Routing: TrivialLayout, where it selects the same physical qubit numbers as virtual and inserts SWAPs to make it work (using StochasticSwap)”

light (1) “Light optimization: Layout/Routing: Layout is first attempted with TrivialLayout. If additional SWAPs are required, a layout with a minimum number of SWAPs is found by using SabreSWAP, then it uses VF2LayoutPostLayout to try to select the best qubits in the graph, InverseCancellation, 1Q gate optimization”

medium (2) “Medium optimization: Layout/Routing: Optimization level 1 (without trivial) + heuristic optimized with greater search depth and trials of optimization function. Because TrivialLayout is not used, there is no attempt to use the same physical and virtual qubit numbers. CommutativeCancellation”

high (3) “High Optimization: Optimization level 2 + heuristic optimized on layout/routing further with greater effort/trials Resynthesis of two-qubit blocks using Cartan’s KAK Decomposition. Unitarity-breaking passes: OptimizeSwapBeforeMeasure: Moves the measurements around to avoid SWAPs RemoveDiagonalGatesBeforeMeasure: Removes gates before measurements that would not effect the measurements”

resilience levels (error mitigation) none (0) level 1 readout error mitigation and measurement twirling using Twirled Readout Error eXtinction (TREX)⁷² level 2 level 1 + gate twirling and zero noise extrapolation (ZNE)^{73–75}

Function fitting 5: all ran with 1000 iterations Function fitting 16: all ran with 1000 iterations
BSE 5: all ran with 1000 iterations BSE 16: all ran with 1000 iterations DDCC

Datasets

In this study, we explore two datasets: a dataset of bond separation energies (BSE) of molecules (Figs. 4a and 4b), where the feature set encodes structural information of each molecule; and a dataset consisting of electronic structure features to predict wave functions using the data-driven coupled-cluster scheme of Townsend and Vogiatzis (Fig. 4c).⁵² We utilize the BSE49 and DDCC databases for two different reasons: the BSE49 database consists of a hard chemical property to predict using few features, while the DDCC dataset can be predicted easily using few features classically but is data intensive in the number of samples per molecule.

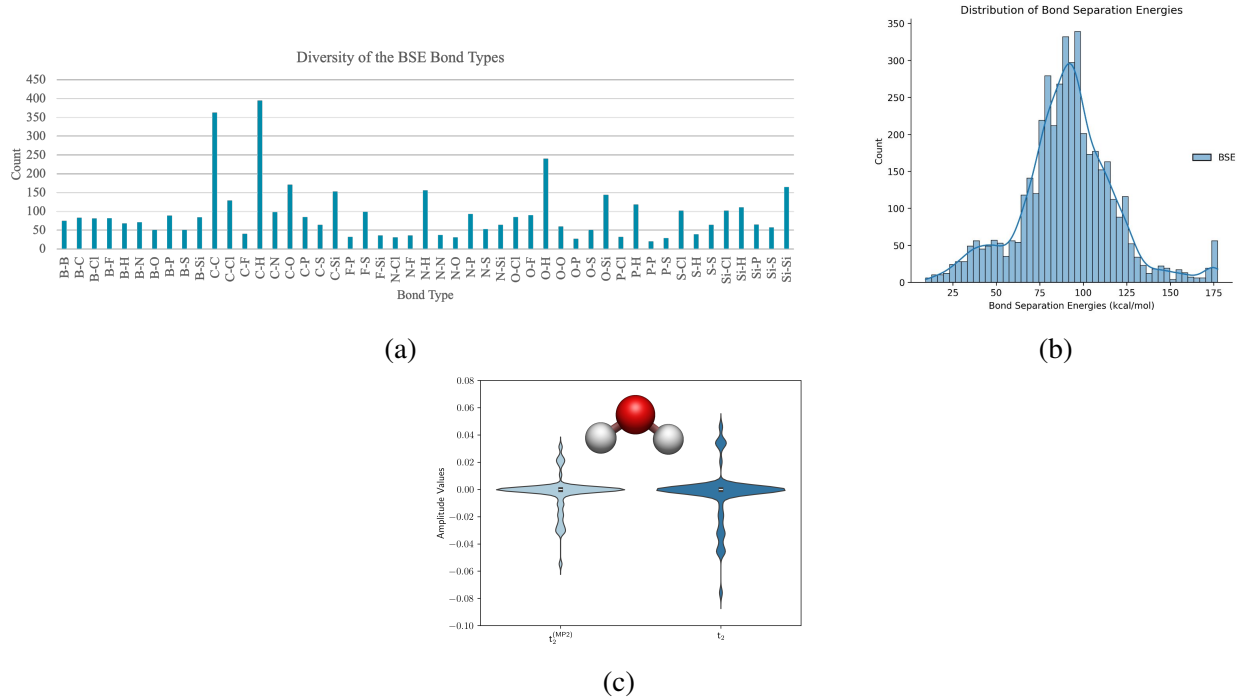


Figure 4: Examples of the datasets explored in this study. For the BSE49 dataset the distributions of the (d) bond types and the (e) bond separation energies in kcal/mol. For the DDCC dataset distributions of the initial MP2 t_2 -amplitudes and the optimized CCSD t_2 -amplitudes are shown in (f).

BSE49 “This work addresses the aforementioned gap in the literature by constructing a large dataset (4502 datapoints) of computationally predicted BSEs of 49 unique bond types, all of which are determined with a high-level composite theoretical procedure denoted as (RO)CBS-QB3. This approach ensures uniform, high-quality reference data and eliminates the need to collect and ver-

ify data gathered from various sources, which may differ substantially in their accuracy. The (RO)CBS-QB3 method is known to produce BDEs of high accuracy. Therefore, it is suitable for developing a database of BSEs that can be used to test and parametrize low-cost computational methods. One particular target application of our dataset is for the training of cost-effective computational approaches like atom-centered potentials (ACPs) or machine learning potentials.” (RO)CBS-QB3^{76–78}

“The structures obtained from the workflow described above were then used for the final step of reference data calculation, using the composite (RO)CBS-QB3^{31,32,33} method. The restricted-open-shell⁶¹ CBS-QB3 or ROCBS-QB3 was employed for the open-shell radical fragments, while restricted closed-shell calculations were performed for the closed-shell parent molecules with CBS-QB3. The composite (RO)CBS-QB3 method approximates energies at the complete-basis-set CCSD(T) level, using a series of computationally lower-cost methods including: (i) geometry optimization followed by vibration frequency calculation using the unrestricted-open-shell⁶² B3LYP/6-311G(2d,d,p) method^{46,47,48,49,50,51,63}, (ii) ROMP2/6-311+G(3d2f,2df,2p) level^{63,64,65} energy extrapolated to the complete-basis-set limit, (iii) energy calculation at ROMP4(SDQ)/6-31+G(d,f,p) level^{63,64,66}, and (iv) energy calculation at ROCCSD(T)/6-31+G \ddagger level^{63,64,67} (where 6-31+G \ddagger is a modified 6-31+G(d) basis set). Note that the final (RO)CBS-QB3 energy includes additional empirical correction terms described in Reference³³. Structures were screened to remove any system for which the imaginary frequencies were obtained. The (RO)CBS-QB3 energies for the structures associated with a particular bond breaking reaction were used to obtain the bond separation energies for the dataset.””

Following model calibration using the function fitting dataset, we explore the applicability of PQCs for complex chemically relevant machine learning tasks. The first chemically motivated dataset we explore is the BSE49 dataset, which contains the bond seperation energies (BSE) for the homolytic bond cleavage of covalently bonded molecules, such as A–B → A \cdot + B \cdot .⁵¹ This dataset consists of 4394 datapoints, 1951 of which are existing and 2443 are hypthoetical structures, with 49 unique A-B single bond types. In practice, we used 2436 of the hypothetical struc-

tures due to issues with valency exceptions when converting to RDKit mol objects which were later used for generating our features for the machine learning models. An important aspect of machine learning in chemistry is the choice of molecular representation, or how the molecule is represented in the machine learning models.⁵⁵ Using RDKit⁷⁹ we examined three commonly applied graph-based molecular representations, Molecular ACCess Systems (MACCS),⁵⁶ Morgan or extended-connectivity fingerprints,^{57,58} and RDKit fingerprints. All three of these methods are use traversals of the molecular graphs to encode various structural details into bit vectors. Lastly, we explore both topology- and physics-based molecular representations, both of which encode the three-dimensional structure of molecules in various, unique ways. Persistent images (PIs) are a topology-based fingerprint that uses persistence homology to encode topological information of three-dimensional molecular structures into fixed dimension images.^{80–82} We use the implementation from Townsend *et al.*,⁸¹ which uses the Ripser Python package to generate PIs.⁸³ Lastly, we explore two physics-based representations, Coulomb matrices (CMs)⁸⁴ and smooth overlap of atomic positions (SOAPs), that were generated using DScribe.⁸⁵ Due to the computational cost of computing the regularized entropy match (REMatch) kernel with the SOAPs representation, we excluded this representation in the overall discussion. We also tested two different methods for representing the components of the bond separation chemical reaction, one where the feature vectors for the products are subtracted from the reactants, denoted by *sub*, similar to the method used in Ref.,⁸⁶ and one that is composed of the reactant molecular only, denoted as *AB*.

Since we are analyzing a diverse set of PQCs, we also examine a diverse set of classic regression models, with varying capabilities, such as ridge, lasso, elastic net, *k*-nearest-neighbors, random forest, gradient boosting, support vector, kernel ridge, and gaussian process regression as implemented in scikit-learn.⁷¹ Based on our results shown in Fig. 5 we found that Morgan fingerprints We found that the best molecular representation across all models test, as shown in Fig. 5, was Morgan fingerprints using the *sub* formulation.

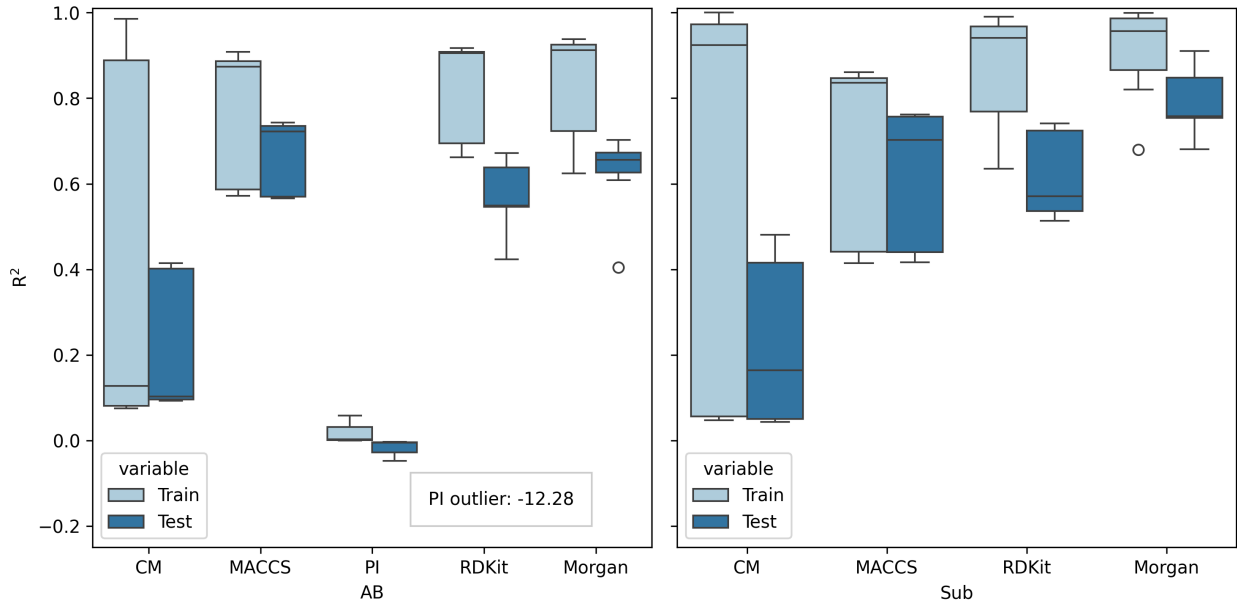


Figure 5: Coulomb matrices (CMs), Molecular ACCess Systems (MACCS), persistence images (PIs), RDKit and Morgan fingerprints. Performance of a diverse set of molecular representations R^2

An additional challenge of applying classical molecular representations for quantum machine learning models is mapping the classical features, often containing hundreds or thousands of features per sample, to the number of qubits used on the quantum device. Initially, the Morgan fingerprints have 2048 features per sample, that need to be reduced down to 5 or 16 qubits. We choose 5 and 16 qubits for two reasons, the first is that these were the standard number of qubits on IBM quantum devices when we started the project and the second is that reducing the number of features reduces the depth of the circuits. To reduce the feature set from 2048 to 5 or 16 features, we explore two different methods, SHapley Additive ExPlanation analysis (SHAP)⁸⁷ and principal component analysis (PCA), as implemented in scikit-learn.⁷¹ Figs. 6b and 6a show the results for the reductions using SHAP and PCA for the training and test set of using 5 and 16 features. The initial model using 2048 features has a train and test mean absolute error (MAE) of 1.91 and 4.98 kcal/mol, with train and test R^2 s of 0.99 and 0.91, respectively. When using SHAP to reduce the feature set size to 5 features, we see that the training set has an MAE of 16.08 kcal/mol and an R^2 of 0.39, while for the test set has an MAE of 15.86 kcal/mol and an R^2 of 0.42. When the

number of features is reduced to 16 features using SHAP, we see slight improvements with train and test MAEs of 10.48 and 11.08 kcal/mol with R^2 s of 0.69 and 0.68, respectively. Using PCA, we see an improvement in accuracy for both 5 and 16 features, where the training sets have MAEs of 4.09 and 3.23 kcal/mol and the test sets have MAEs of 10.17 and 8.40 kcal/mol, respectively. The R^2 s for PCA with 5 and 16 features also shows improvement over the reductions using SHAP, with R^2 s of 0.95 and 0.69 for the training and test set, respectively, using 5 features and 0.97 and 0.78 for the training and test set, respectively, using 16 features. Due to the increased performance, despite exhibiting overfitting, we choose to use Morgan fingerprints reduced using PCA for our QML models.

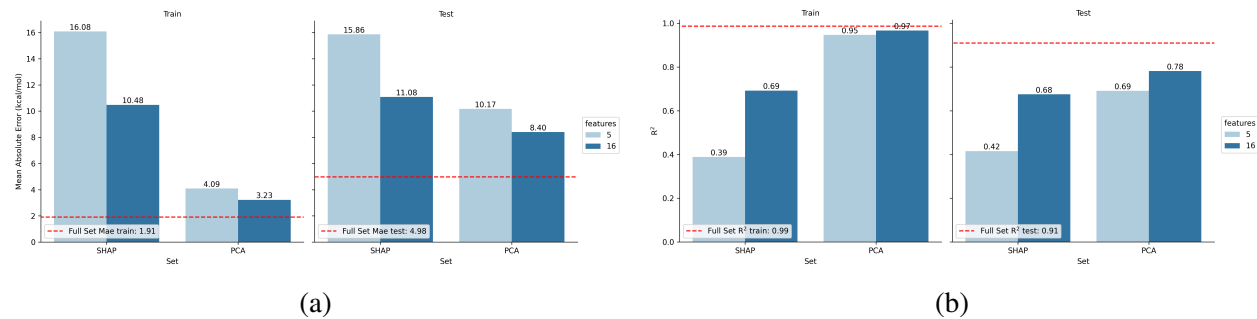


Figure 6: Feature reduction of the BSE dataset represented using

The next chemical dataset explored is based on the data-driven coupled-cluster (DDCC) method, which is a machine learning-based approach for accelerating the convergence of coupled-cluster singles and doubles (CCSD) calculations.^{52,53} This method works by predicting the t_2 -amplitudes of the CCSD wave function (Eq. 10) with features generated using lower-level methods, such as Hartree-Fock (HF) and Møller-Plesset second-order perturbation theory (MP2), which are used to initialize CCSD calculations.

The coupled-cluster wave function takes the general form,

$$|\Psi_{\text{CC}}\rangle = \exp(\hat{T}) |\Psi_0\rangle \quad (10)$$

where the cluster operator is denoted as \hat{T} and the reference, Hartree-Fock wave function is denoted

as $|\Psi_0\rangle$. The CCSD wave function truncates the cluster operator to only include singles and doubles excitations. The CCSD correlation energy is defined as,

$$E_{\text{corr}}^{\text{CCSD}} = \sum_{\substack{a < b \\ i < j}} \langle ij || ab \rangle t_{ij}^{ab} + \sum_{\substack{a < b \\ i < j}} \langle ij || ab \rangle t_i^a t_j^b \quad (11)$$

where i and j denote occupied orbitals, a and b denote virtual orbitals, t_{ij}^{ab} are the t_2 -amplitudes which correspond to two-electron excitations, t_i^a and t_j^b are t_1 -amplitudes corresponding to one-electron excitations, and $\langle ij || ab \rangle$ are two-electron integrals.

For each two-electron excitation, t_{ij}^{ab} , a feature set can be generated from HF and MP2. The feature set includes the MP2 t_2 -amplitudes, which are used to initialize the CCSD amplitudes,

$$t_{ij(\text{MP2})}^{ab} = \frac{\langle ij || ab \rangle}{\varepsilon_i + \varepsilon_j - \varepsilon_a - \varepsilon_b} \quad (12)$$

where ε_i and ε_j denote the orbital energies of the occupied orbitals i and j , while the virtual orbitals a and b are denoted by ε_a and ε_b . Features related to the MP2 t_2 -amplitudes that are also included in the feature set are the numerator ($\langle ij || ab \rangle$) and denominator ($\varepsilon_i + \varepsilon_j - \varepsilon_a - \varepsilon_b$), a binary feature to denote whether the excitation goes to the same virtual orbital, and the orbital energies ($\varepsilon_i, \varepsilon_j, \varepsilon_a, \varepsilon_b$). The feature set also includes terms related to the individual contributes to the orbital energies are also included, such as the one-electron Hamiltonian (h), Coulombic matrix (J), and exchange matrix K , and Coulombic and exchange integrals ($J_a^i, J_b^j, K_i^a, K_j^b$). In total, there are 30 features for each t_2 -amplitude due to the addition of features that denote the sign and magnitudes of the previously mentioned features.

Our dataset consists of 199 water molecules from the study by Townsend and Vogiatzis using the STO-3G basis set⁸⁸ and frozen core orbitals. All data was generated using Psi4⁸⁹ and Psi4Numpy.⁹⁰ As previously mentioned, the DDCC method is data intensive regarding the number of samples per molecule, for example, each water molecule has 4 occupied and 2 virtual orbitals. The number of t_2 -amplitudes is equivalent to $(N_{\text{occ}})^2(N_{\text{virt}})^2$, where N_{occ} denotes the number of oc-

cupied orbitals and N_{virt} denotes the number of virtual orbitals, so the total number of t_2 -amplitudes per molecule is 64. Further details regarding the feature set and implementation can be found in⁵²

Like the BSE dataset, the 30 features from the full DDCC feature set must be reduced to 5 or 16 features using SHAP or PCA. Unlike the BSE dataset, we choose SHAP over PCA for the feature reduction since there is a direct correlation between the input features and output values. As shown in Fig. 7, 5 and 16 features can accurately recover performance of the original model using 30 features, where all three models have train and test R²s of 1.00. Due to the computational costs of running QML models, we will then use only 5 features for all DDCC QML models. The 5 most important features are the two-electron integrals ($\langle ij||ab\rangle$), MP2 t_2 -amplitudes ($t_{ij}^{ab}_{(MP2)}$), the magnitude of the MP2 t_2 -amplitudes, and the difference in orbital energies ($\epsilon_i + \epsilon_j - \epsilon_a - \epsilon_b$).

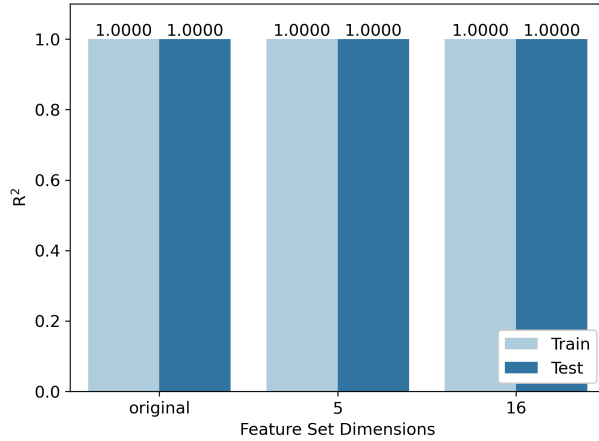


Figure 7

3 Results and Discussion

BSE

To explore the performance of PQCs for chemically relevant datasets, the dataset we explore is the BSE49 dataset, which consists of a diverse set of bond separation energies and the related structures, as highlighted in Figs. 4a and 4b. Initially, we study the five qubit data, Figs. 8a and 8b, due to computational considerations.

five qubit best encoder-ansatz pair: train R²/test R² Best encoder on average train R²/test R²

Best ansatz on average train R²/test R²

'M-M-CNOT', '-0.0216' 'Full-CRX', '0.1214'

sixteen qubit 8c 8d removed the really bad ones from five qubit best encoder-ansatz pair: train

R²/test R² Best encoder on average train R²/test R² Best ansatz on average train R²/test R²

Talk about the cost of going wider, and inherently deeper

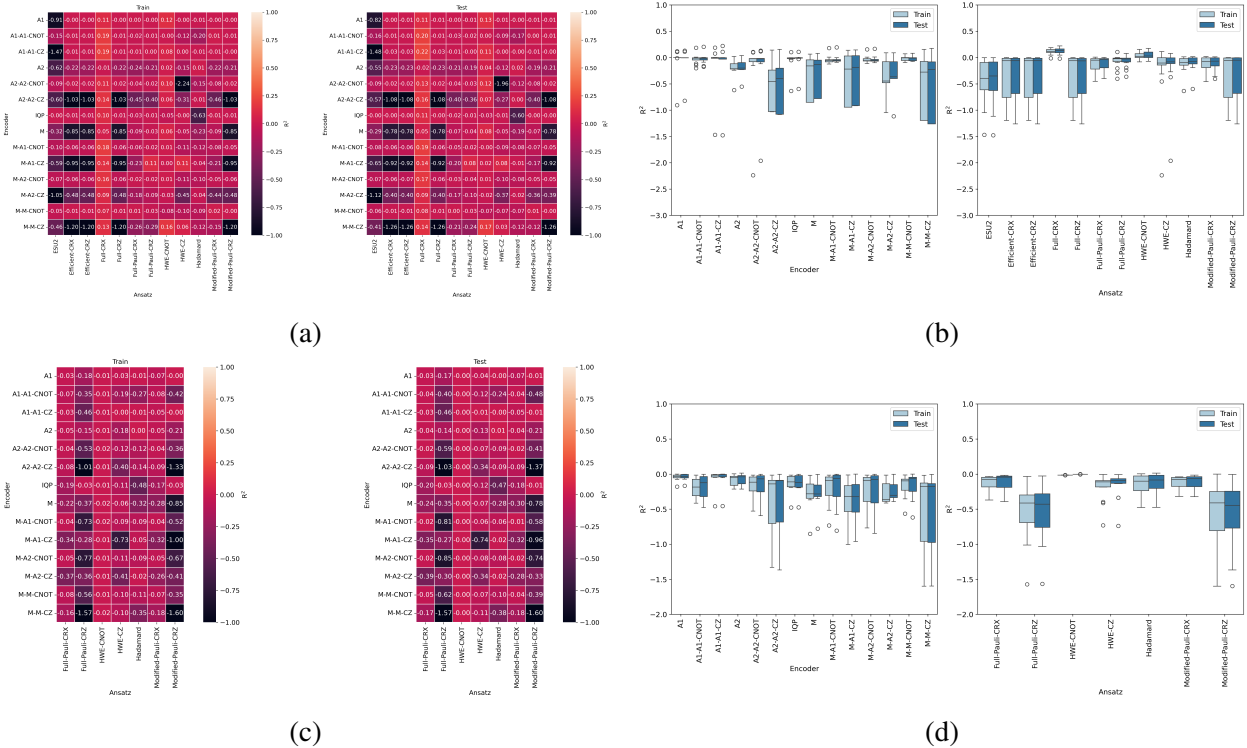


Figure 8

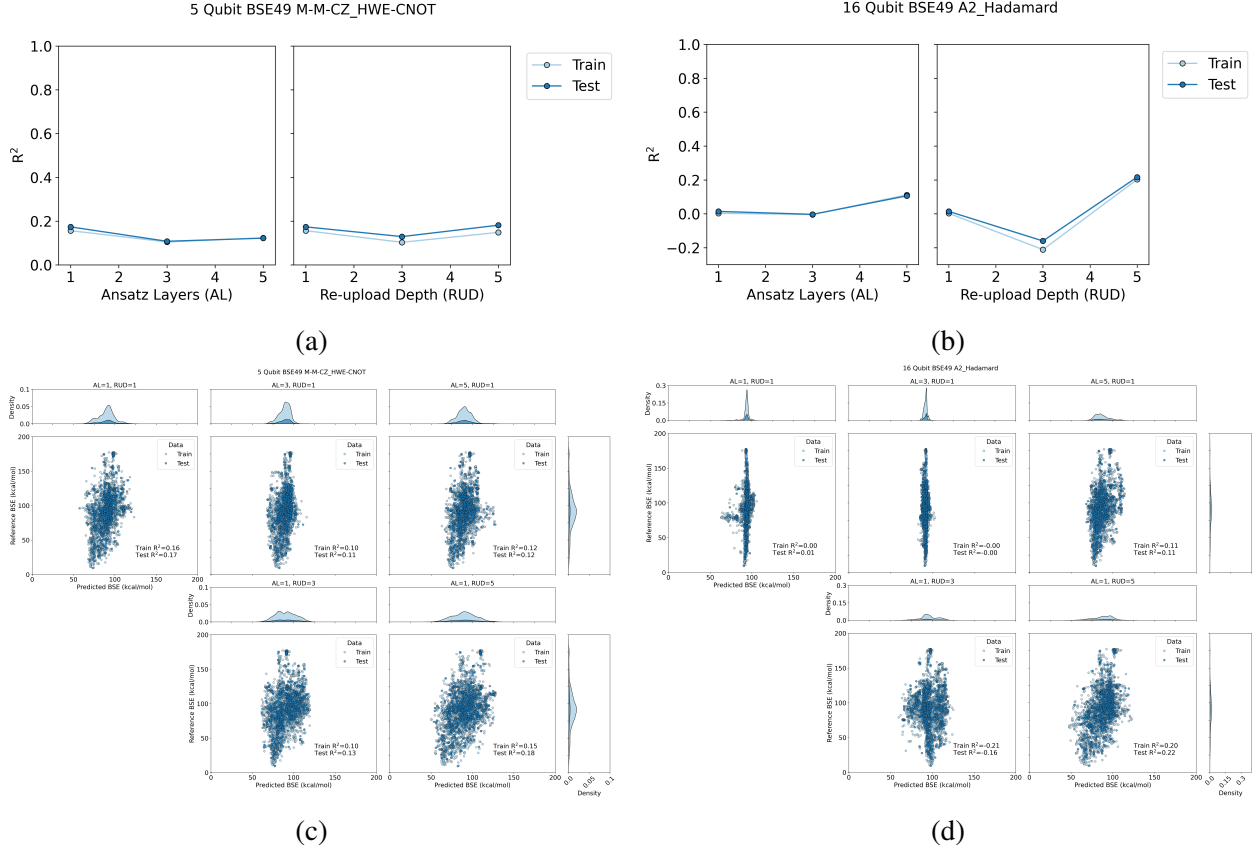


Figure 9

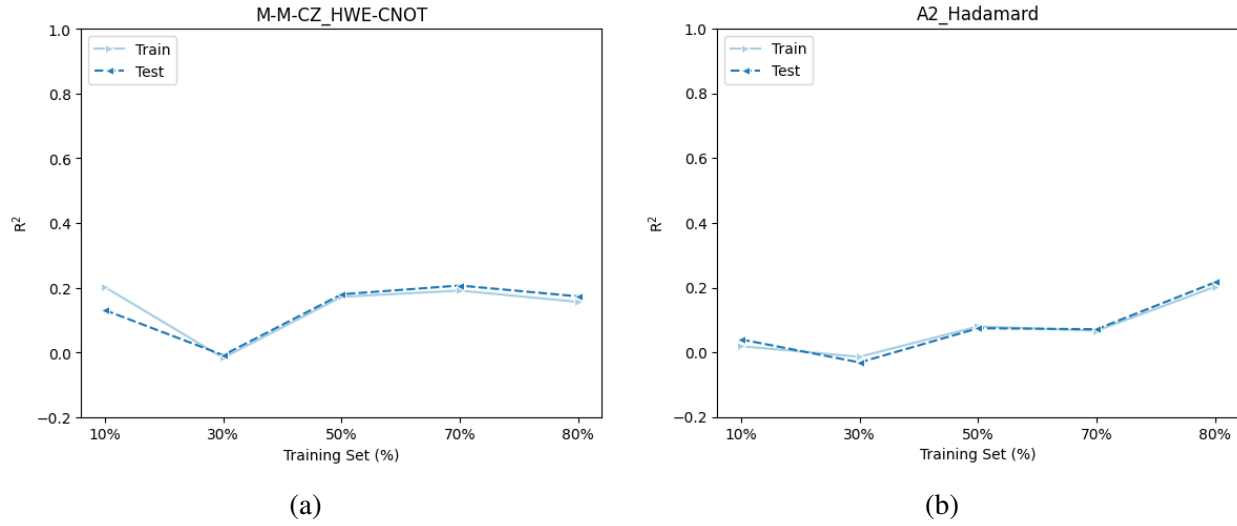


Figure 10

DDCC

Structure

- Broad set
- RUD/AL tests
- learning curve (maybe)
- real device

A2_HWE-CNOT Train R^2 0.62/test R^2 0.62 Best encoder average Train R^2 X/test R^2 Y Best ansatz HWE-CNOT average Train R^2 X/test R^2 Y

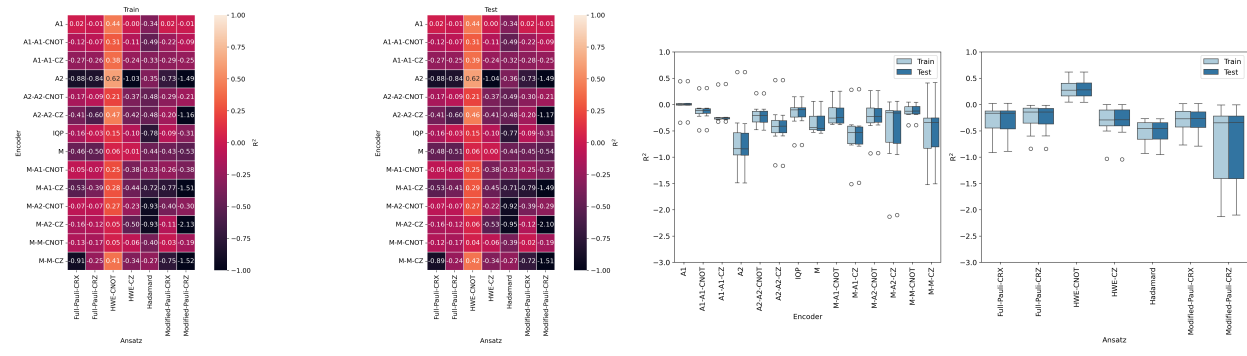


Figure 11

(AL,RUD)=(1,1) Train R^2 0.62/test R^2 0.62 (AL,RUD)=(1,3) Train R^2 0.85/test R^2 0.85 (AL,RUD)=(1,5) Train R^2 0.82/test R^2 0.83 (AL,RUD)=(3,1) Train R^2 0.71/test R^2 0.71 (AL,RUD)=(5,1) Train R^2 0.77/test R^2 0.77

Talk about the cost of going wider, and inherently deeper

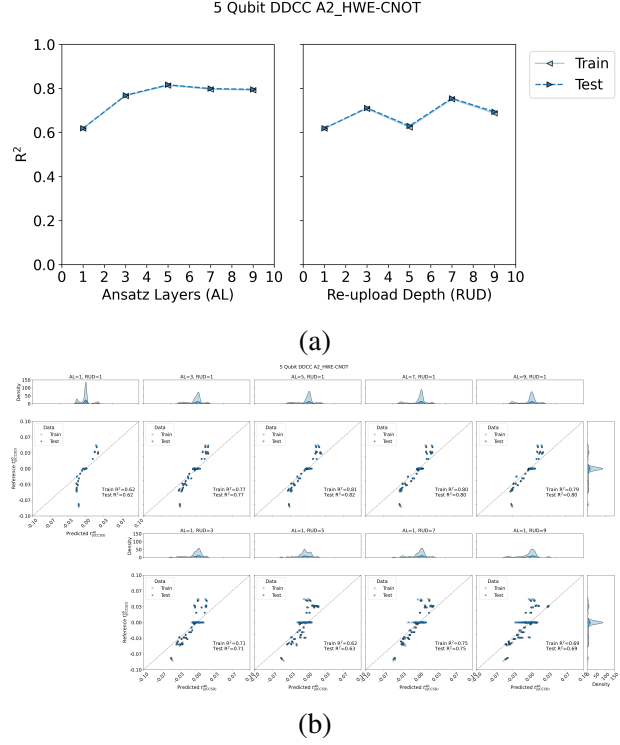


Figure 12: Model evaluation, using R^2 (y-axis), of re-upload depths (RUD) and ansatz layers (AL) of 1, 3, and 5 for the A2_HWE-CNOT using the DDCC dataset. The left side of the plot denotes the training set and the right side the test set.

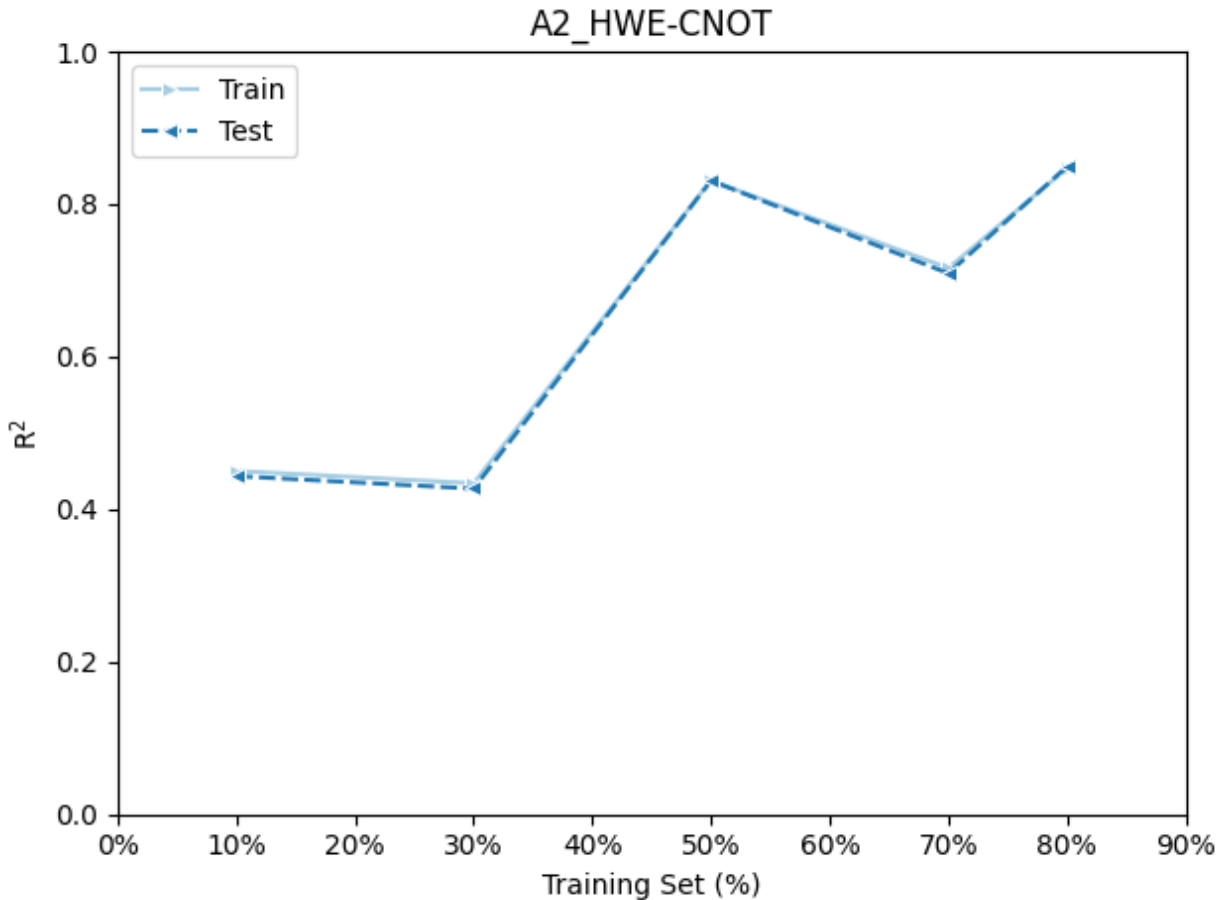


Figure 13

Ansaetze analysis⁶⁸ “In particular, a substantial improvement in performance of two-qubit gates in a ring or all-to-all connected arrangement, compared to that of those on a line, is observed.”

“Furthermore, improvement in both descriptors is achieved by sequences of controlled X-rotation gates compared to sequences of controlled Z-rotation gates.”

“investigated how expressibility “saturates” with increased circuit depth, finding that the rate and saturated value appear to be distinguishing features of a PQC”

5 qubit/5 ansatz layers: $2*5 + 3 * 5 * 5 = 85$ parameters (75 trainable, $5 * 2$ features) A2 $2n$ parameters HWE-CNOT $3nL$ parameters 2 qubit gates nL Number of parameters $(2n+3nL)=(2+3L)*n$
 n , number of qubits and L , number of circuit layers

To efficiently run DDCC on IBM Quebec, splitting the data into batches of ≈ 4 samples with 64 t_2 -amplitudes each.

One iteration would require approximately $N_{\text{samples}} * N_{\text{occ}}^2 * N_{\text{virt}}^2 * N_{\text{shots}} * N_{\text{observables}}$ circuit executions (+ whatever SPSA costs to run per iteration)

Ran using the state vector model parameters for one iteration to test the optimization and resilience levels using Fake Quebec before running on the real device

$$\{1024 \times x | x \in [1, 10]\}$$

Fake Optimization level 2 resilience level 0

Regarding the number of circuit executions vs performance 3072 (1024 times 3) is the best number of shots

Fig. S1 Fig. S2

Real Optimization level 2 resilience level 1 3072

resilience level 2 is too expensive on the real device Regarding the number of circuit executions vs performance 3072 (1024 times 3) is the best number of shots

Error handling for real run with iter>1

4 Conclusion

Quantum advantage in terms of computational complexity but not in model performance?

Depth is not always better! Molecular representations specifically for QML Distributed QC to incorporate more features Noiseless simulation is costly and does not offer the desired accuracy for BSE49 or DDCC

DDCC could be a useful dataset to benchmark PQC models since it is trivial to perform classically, yet hard for PQCs...

References

- (1) Janet, J. P.; Kulik, H. J. *Machine Learning in Chemistry*; ACS In Focus; American Chemical Society, 2020.

- (2) Behler, J. Perspective: Machine learning potentials for atomistic simulations. *JOURNAL OF CHEMICAL PHYSICS* **2016**, *145*.
- (3) S. Smith, J.; Isayev, O.; E. Roitberg, A. ANI-1: an extensible neural network potential with DFT accuracy at force field computational cost. *Chemical Science* **2017**, *8*, 3192–3203, Publisher: Royal Society of Chemistry.
- (4) Gao, X.; Ramezanghorbani, F.; Isayev, O.; Smith, J. S.; Roitberg, A. E. TorchANI: A Free and Open Source PyTorch-Based Deep Learning Implementation of the ANI Neural Network Potentials. *J. Chem. Inf. Model.* **2020**, *60*, 3408–3415, Publisher: American Chemical Society.
- (5) Yang, K.; Swanson, K.; Jin, W.; Coley, C.; Eiden, P.; Gao, H.; Guzman-Perez, A.; Hopper, T.; Kelley, B.; Mathea, M.; Palmer, A.; Settels, V.; Jaakkola, T.; Jensen, K.; Barzilay, R. Analyzing Learned Molecular Representations for Property Prediction. *JOURNAL OF CHEMICAL INFORMATION AND MODELING* **2019**, *59*, 3370–3388.
- (6) Ramakrishnan, R.; Dral, P. O.; Rupp, M.; von Lilienfeld, O. A. Quantum chemistry structures and properties of 134 kilo molecules. *SCIENTIFIC DATA* **2014**, *1*.
- (7) Ramakrishnan, R.; Dral, P. O.; Rupp, M.; von Lilienfeld, O. A. Big Data Meets Quantum Chemistry Approximations: The \$\Delta\$-Machine Learning Approach. *JOURNAL OF CHEMICAL THEORY AND COMPUTATION* **2015**, *11*, 2087–2096.
- (8) Hansen, K.; Biegler, F.; Ramakrishnan, R.; Pronobis, W.; von Lilienfeld, O. A.; Mueller, K.-R.; Tkatchenko, A. Machine Learning Predictions of Molecular Properties: Accurate Many-Body Potentials and Nonlocality in Chemical Space. *JOURNAL OF PHYSICAL CHEMISTRY LETTERS* **2015**, *6*, 2326–2331.
- (9) Unke, O. T.; Meuwly, M. PhysNet: A Neural Network for Predicting Energies, Forces, Dipole Moments, and Partial Charges. *JOURNAL OF CHEMICAL THEORY AND COMPUTATION* **2019**, *15*, 3678–3693.

- (10) Zhong, M. et al. Accelerated discovery of CO₂ electrocatalysts using active machine learning. *NATURE* **2020**, *581*, 178+.
- (11) Nandy, A.; Duan, C.; Taylor, M. G.; Liu, F.; Steeves, A. H.; Kulik, H. J. Computational Discovery of Transition-metal Complexes: From High-throughput Screening to Machine Learning. *Chem. Rev.* **2021**, *121*, 9927–10000, Publisher: American Chemical Society.
- (12) M. Jones, G.; A. Smith, B.; K. Kirkland, J.; D. Vogiatzis, K. Data-driven ligand field exploration of Fe(iv)–oxo sites for C–H activation. *Inorganic Chemistry Frontiers* **2023**, *10*, 1062–1075, Publisher: Royal Society of Chemistry.
- (13) Goh, G. B.; Hodas, N. O.; Vishnu, A. Deep learning for computational chemistry. *JOURNAL OF COMPUTATIONAL CHEMISTRY* **2017**, *38*, 1291–1307.
- (14) Yang, X.; Wang, Y.; Byrne, R.; Schneider, G.; Yang, S. Concepts of Artificial Intelligence for Computer-Assisted Drug Discovery. *Chem. Rev.* **2019**, *119*, 10520–10594, Publisher: American Chemical Society.
- (15) Butler, K. T.; Davies, D. W.; Cartwright, H.; Isayev, O.; Walsh, A. Machine learning for molecular and materials science. *NATURE* **2018**, *559*, 547–555.
- (16) Sanchez-Lengeling, B.; Aspuru-Guzik, A. Inverse molecular design using machine learning: Generative models for matter engineering. *SCIENCE* **2018**, *361*, 360–365.
- (17) Raccuglia, P.; Elbert, K. C.; Adler, P. D. F.; Falk, C.; Wenny, M. B.; Mollo, A.; Zeller, M.; Friedler, S. A.; Schrier, J.; Norquist, A. J. Machine-learning-assisted materials discovery using failed experiments. *NATURE* **2016**, *533*, 73+.
- (18) Ufimtsev, I. S.; Martínez, T. J. Graphical Processing Units for Quantum Chemistry. *Computing in Science & Engineering* **2008**, *10*, 26–34, Conference Name: Computing in Science & Engineering.

- (19) Götz, A. W.; Wölfle, T.; Walker, R. C. In *Annual Reports in Computational Chemistry*; Wheeler, R. A., Ed.; Elsevier, 2010; Vol. 6; pp 21–35.
- (20) Pederson, R.; Kozlowski, J.; Song, R.; Beall, J.; Ganahl, M.; Hauru, M.; Lewis, A. G. M.; Yao, Y.; Mallick, S. B.; Blum, V.; Vidal, G. Large Scale Quantum Chemistry with Tensor Processing Units. *J. Chem. Theory Comput.* **2023**, *19*, 25–32, Publisher: American Chemical Society.
- (21) Gawehn, E.; Hiss, J. A.; Brown, J. B.; Schneider, G. Advancing drug discovery via GPU-based deep learning. *Expert Opinion on Drug Discovery* **2018**, *13*, 579–582, Publisher: Taylor & Francis _eprint: <https://doi.org/10.1080/17460441.2018.1465407>.
- (22) Pandey, M.; Fernandez, M.; Gentile, F.; Isayev, O.; Tropsha, A.; Stern, A. C.; Cherkasov, A. The transformational role of GPU computing and deep learning in drug discovery. *Nat Mach Intell* **2022**, *4*, 211–221, Publisher: Nature Publishing Group.
- (23) Cao, Y.; Romero, J.; Olson, J. P.; Degroote, M.; Johnson, P. D.; Kieferová, M.; Kivlichan, I. D.; Menke, T.; Peropadre, B.; Sawaya, N. P. D.; Sim, S.; Veis, L.; Aspuru-Guzik, A. Quantum Chemistry in the Age of Quantum Computing. *Chem. Rev.* **2019**, *119*, 10856–10915, Publisher: American Chemical Society.
- (24) Abrams, D. S.; Lloyd, S. Simulation of many-body Fermi systems on a universal quantum computer. *Physical Review Letters* **1997**, *79*, 2586, Publisher: APS.
- (25) Abrams, D. S.; Lloyd, S. Quantum algorithm providing exponential speed increase for finding eigenvalues and eigenvectors. *Physical Review Letters* **1999**, *83*, 5162, Publisher: APS.
- (26) Aspuru-Guzik, A.; Dutoi, A. D.; Love, P. J.; Head-Gordon, M. Simulated quantum computation of molecular energies. *Science* **2005**, *309*, 1704–1707, Publisher: American Association for the Advancement of Science.

- (27) Lanyon, B. P.; Whitfield, J. D.; Gillett, G. G.; Goggin, M. E.; Almeida, M. P.; Kassal, I.; Biamonte, J. D.; Mohseni, M.; Powell, B. J.; Barbieri, M.; others Towards quantum chemistry on a quantum computer. *Nature chemistry* **2010**, *2*, 106–111, Publisher: Nature Publishing Group.
- (28) Whitfield, J. D.; Biamonte, J.; Aspuru-Guzik, A. Simulation of electronic structure Hamiltonians using quantum computers. *Molecular Physics* **2011**, *109*, 735–750, Publisher: Taylor & Francis.
- (29) Aspuru-Guzik, A.; Walther, P. Photonic quantum simulators. *Nature physics* **2012**, *8*, 285–291, Publisher: Nature Publishing Group.
- (30) Peruzzo, A.; McClean, J.; Shadbolt, P.; Yung, M.-H.; Zhou, X.-Q.; Love, P. J.; Aspuru-Guzik, A.; O’Brien, J. L. A variational eigenvalue solver on a photonic quantum processor. *Nat Commun* **2014**, *5*, 4213, Publisher: Nature Publishing Group.
- (31) Cerezo, M.; Arrasmith, A.; Babbush, R.; Benjamin, S. C.; Endo, S.; Fujii, K.; McClean, J. R.; Mitarai, K.; Yuan, X.; Cincio, L.; Coles, P. J. Variational quantum algorithms. *Nat Rev Phys* **2021**, *3*, 625–644, Publisher: Nature Publishing Group.
- (32) McClean, J. R.; Romero, J.; Babbush, R.; Aspuru-Guzik, A. The theory of variational hybrid quantum-classical algorithms. *New J. Phys.* **2016**, *18*, 023023, Publisher: IOP Publishing.
- (33) Bharti, K.; Cervera-Lierta, A.; Kyaw, T. H.; Haug, T.; Alperin-Lea, S.; Anand, A.; Degroote, M.; Heimonen, H.; Kottmann, J. S.; Menke, T.; Mok, W.-K.; Sim, S.; Kwek, L.-C.; Aspuru-Guzik, A. Noisy intermediate-scale quantum algorithms. *Rev. Mod. Phys.* **2022**, *94*, 015004, Publisher: American Physical Society.
- (34) Romero, J.; Babbush, R.; McClean, J. R.; Hempel, C.; Love, P. J.; Aspuru-Guzik, A. Strategies for quantum computing molecular energies using the unitary coupled cluster ansatz. *QUANTUM SCIENCE AND TECHNOLOGY* **2019**, *4*.

- (35) McArdle, S.; Endo, S.; Aspuru-Guzik, A.; Benjamin, S.; Yuan, X. Quantum computational chemistry. *REVIEWS OF MODERN PHYSICS* **2020**, *92*.
- (36) Bauer, B.; Bravyi, S.; Motta, M.; Chan, G. K.-L. Quantum Algorithms for Quantum Chemistry and Quantum Materials Science. *CHEMICAL REVIEWS* **2020**, *120*, 12685–12717.
- (37) Biamonte, J.; Wittek, P.; Pancotti, N.; Rebentrost, P.; Wiebe, N.; Lloyd, S. Quantum machine learning. *Nature* **2017**, *549*, 195–202.
- (38) Benedetti, M.; Lloyd, E.; Sack, S.; Fiorentini, M. Parameterized quantum circuits as machine learning models. *Quantum Sci. Technol.* **2019**, *4*, 043001.
- (39) Suzuki, T.; Katouda, M. Predicting toxicity by quantum machine learning. *J. Phys. Commun.* **2020**, *4*, 125012.
- (40) Smaldone, A. M.; Batista, V. S. Quantum-to-Classical Neural Network Transfer Learning Applied to Drug Toxicity Prediction. *J. Chem. Theory Comput.* **2024**, *20*, 4901–4908, Publisher: American Chemical Society.
- (41) Bhatia, A. S.; Saggi, M. K.; Kais, S. Quantum Machine Learning Predicting ADME-Tox Properties in Drug Discovery. *J. Chem. Inf. Model.* **2023**, *63*, 6476–6486, Publisher: American Chemical Society.
- (42) Kao, P.-Y.; Yang, Y.-C.; Chiang, W.-Y.; Hsiao, J.-Y.; Cao, Y.; Aliper, A.; Ren, F.; Aspuru-Guzik, A.; Zhavoronkov, A.; Hsieh, M.-H.; Lin, Y.-C. Exploring the Advantages of Quantum Generative Adversarial Networks in Generative Chemistry. *J. Chem. Inf. Model.* **2023**, *63*, 3307–3318, Publisher: American Chemical Society.
- (43) Li, J.; Topaloglu, R. O.; Ghosh, S. Quantum Generative Models for Small Molecule Drug Discovery. *IEEE Transactions on Quantum Engineering* **2021**, *2*, 1–8, Conference Name: IEEE Transactions on Quantum Engineering.

- (44) Avramouli, M.; Savvas, I.; Vasilaki, A.; Garani, G.; Xenakis, A. Quantum Machine Learning in Drug Discovery: Current State and Challenges. Proceedings of the 26th Pan-Hellenic Conference on Informatics. New York, NY, USA, 2023; pp 394–401.
- (45) Avramouli, M.; Savvas, I. K.; Vasilaki, A.; Garani, G. Unlocking the Potential of Quantum Machine Learning to Advance Drug Discovery. *Electronics* **2023**, *12*, 2402, Number: 11 Publisher: Multidisciplinary Digital Publishing Institute.
- (46) Ishiyama, Y.; Nagai, R.; Mieda, S.; Takei, Y.; Minato, Y.; Natsume, Y. Noise-robust optimization of quantum machine learning models for polymer properties using a simulator and validated on the IonQ quantum computer. *Sci Rep* **2022**, *12*, 19003, Publisher: Nature Publishing Group.
- (47) Ryu, J.-Y.; Elala, E.; Rhee, J.-K. K. Quantum Graph Neural Network Models for Materials Search. *Materials* **2023**, *16*, 4300, Number: 12 Publisher: Multidisciplinary Digital Publishing Institute.
- (48) Vitz, M.; Mohammadbagherpoor, H.; Sandeep, S.; Vlasic, A.; Padbury, R.; Pham, A. Hybrid Quantum Graph Neural Network for Molecular Property Prediction. 2024; <http://arxiv.org/abs/2405.05205>, arXiv:2405.05205 [quant-ph].
- (49) Jin, H.; Merz, K. M. J. Integrating Machine Learning and Quantum Circuits for Proton Affinity Predictions. *J. Chem. Theory Comput.* **2025**, Publisher: American Chemical Society.
- (50) Hatakeyama-Sato, K.; Igarashi, Y.; Kashikawa, T.; Kimura, K.; Oyaizu, K. Quantum circuit learning as a potential algorithm to predict experimental chemical properties. *Digital Discovery* **2023**, *2*, 165–176.
- (51) Prasad, V. K.; Khalilian, M. H.; Otero-de-la Roza, A.; DiLabio, G. A. BSE49, a diverse, high-quality benchmark dataset of separation energies of chemical bonds. *Sci Data* **2021**, *8*, 300, Publisher: Nature Publishing Group.

- (52) Townsend, J.; Vogiatzis, K. D. Data-Driven Acceleration of the Coupled-Cluster Singles and Doubles Iterative Solver. *J. Phys. Chem. Lett.* **2019**, *10*, 4129–4135.
- (53) Jones, G. M.; S. Pathirage, P. D. V.; Vogiatzis, K. D. In *Quantum Chemistry in the Age of Machine Learning*; Dral, P. O., Ed.; Elsevier, 2023; pp 509–529.
- (54) Cerezo, M.; Verdon, G.; Huang, H.-Y.; Cincio, L.; Coles, P. J. Challenges and opportunities in quantum machine learning. *Nat Comput Sci* **2022**, *2*, 567–576, Publisher: Nature Publishing Group.
- (55) Jones, G. M.; Story, B.; Maroulas, V.; Vogiatzis, K. D. *Molecular Representations for Machine Learning*; ACS In Focus; American Chemical Society, 2023.
- (56) Durant, J. L.; Leland, B. A.; Henry, D. R.; Nourse, J. G. Reoptimization of MDL Keys for Use in Drug Discovery. *Journal of Chemical Information and Computer Sciences* **2002**, *42*, 1273–1280.
- (57) Morgan, H. L. The Generation of a Unique Machine Description for Chemical Structures-A Technique Developed at Chemical Abstracts Service. *Journal of Chemical Documentation* **1965**, *5*, 107–113, Type: Journal Article.
- (58) Rogers, D.; Hahn, M. Extended-connectivity fingerprints. *Journal of Chemical Information and Modeling* **2010**, *50*, 742–754, Publisher: American Chemical Society.
- (59) Bergholm, V. et al. PennyLane: Automatic differentiation of hybrid quantum-classical computations. 2022; <http://arxiv.org/abs/1811.04968>, arXiv:1811.04968 [quant-ph].
- (60) Javadi-Abhari, A.; Treinish, M.; Krsulich, K.; Wood, C. J.; Lishman, J.; Gacon, J.; Martiel, S.; Nation, P. D.; Bishop, L. S.; Cross, A. W.; Johnson, B. R.; Gambetta, J. M. Quantum computing with Qiskit. 2024; _eprint: 2405.08810.
- (61) Pérez-Salinas, A.; Cervera-Lierta, A.; Gil-Fuster, E.; Latorre, J. I. Data re-uploading for a

- universal quantum classifier. *Quantum* **2020**, *4*, 226, Publisher: Verein zur Förderung des Open Access Publizierens in den Quantenwissenschaften.
- (62) Mitarai, K.; Negoro, M.; Kitagawa, M.; Fujii, K. Quantum circuit learning. *Phys. Rev. A* **2018**, *98*, 032309.
- (63) Bremner, M. J.; Montanaro, A.; Shepherd, D. J. Average-case complexity versus approximate simulation of commuting quantum computations. *Phys. Rev. Lett.* **2016**, *117*, 080501, arXiv:1504.07999 [quant-ph].
- (64) Havlicek, V.; Córcoles, A. D.; Temme, K.; Harrow, A. W.; Kandala, A.; Chow, J. M.; Gambetta, J. M. Supervised learning with quantum enhanced feature spaces. *Nature* **2019**, *567*, 209–212, arXiv:1804.11326 [quant-ph].
- (65) Stoudenmire, E.; Schwab, D. J. Supervised Learning with Tensor Networks. Advances in Neural Information Processing Systems. 2016.
- (66) Lund, A. P.; Bremner, M. J.; Ralph, T. C. Quantum sampling problems, BosonSampling and quantum supremacy. *npj Quantum Inf* **2017**, *3*, 1–8, Publisher: Nature Publishing Group.
- (67) Harrow, A. W.; Montanaro, A. Quantum computational supremacy. *Nature* **2017**, *549*, 203–209, Publisher: Nature Publishing Group.
- (68) Sim, S.; Johnson, P. D.; Aspuru-Guzik, A. Expressibility and Entangling Capability of Parameterized Quantum Circuits for Hybrid Quantum-Classical Algorithms. *Advanced Quantum Technologies* **2019**, *2*, 1900070.
- (69) Suzuki, Y. et al. Qulacs: a fast and versatile quantum circuit simulator for research purpose. *Quantum* **2021**, *5*, 559, arXiv:2011.13524 [quant-ph].
- (70) Virtanen, P. et al. SciPy 1.0: Fundamental Algorithms for Scientific Computing in Python. *Nature Methods* **2020**, *17*, 261–272.

- (71) Pedregosa, F. et al. Scikit-learn: Machine Learning in Python. *Journal of Machine Learning Research* **2011**, *12*, 2825–2830.
- (72) van den Berg, E.; Minev, Z. K.; Temme, K. Model-free readout-error mitigation for quantum expectation values. *Phys. Rev. A* **2022**, *105*, 032620, Publisher: American Physical Society.
- (73) Kandala, A.; Temme, K.; Córcoles, A. D.; Mezzacapo, A.; Chow, J. M.; Gambetta, J. M. Error mitigation extends the computational reach of a noisy quantum processor. *Nature* **2019**, *567*, 491–495, Publisher: Nature Publishing Group.
- (74) Li, Y.; Benjamin, S. C. Efficient Variational Quantum Simulator Incorporating Active Error Minimization. *Phys. Rev. X* **2017**, *7*, 021050, Publisher: American Physical Society.
- (75) Temme, K.; Bravyi, S.; Gambetta, J. M. Error Mitigation for Short-Depth Quantum Circuits. *Phys. Rev. Lett.* **2017**, *119*, 180509, Publisher: American Physical Society.
- (76) Wood, G. P. F.; Radom, L.; Petersson, G. A.; Barnes, E. C.; Frisch, M. J.; Montgomery, J. A., Jr. A restricted-open-shell complete-basis-set model chemistry. *The Journal of Chemical Physics* **2006**, *125*, 094106.
- (77) Montgomery, J. A., Jr.; Frisch, M. J.; Ochterski, J. W.; Petersson, G. A. A complete basis set model chemistry. VI. Use of density functional geometries and frequencies. *The Journal of Chemical Physics* **1999**, *110*, 2822–2827.
- (78) Montgomery, J. A., Jr.; Frisch, M. J.; Ochterski, J. W.; Petersson, G. A. A complete basis set model chemistry. VII. Use of the minimum population localization method. *The Journal of Chemical Physics* **2000**, *112*, 6532–6542.
- (79) RDKit. <https://www.rdkit.org/>.
- (80) Adams, H.; Emerson, T.; Kirby, M.; Neville, R.; Peterson, C.; Shipman, P.; Chepush-tanova, S.; Hanson, E.; Motta, F.; Ziegelmeier, L. Persistence Images: A Stable Vector Representation of Persistent Homology. *Journal of Machine Learning Research* **2017**, *18*, 1–35.

- (81) Townsend, J.; Micucci, C. P.; Hymel, J. H.; Maroulas, V.; Vogiatzis, K. D. Representation of molecular structures with persistent homology for machine learning applications in chemistry. *Nature Communications* **2020**, *11*, 3230, Publisher: Nature Research.
- (82) Schiff, Y.; Chenthamarakshan, V.; Hoffman, S. C.; Natesan Ramamurthy, K.; Das, P. Augmenting Molecular Deep Generative Models with Topological Data Analysis Representations. ICASSP 2022 - 2022 IEEE International Conference on Acoustics, Speech and Signal Processing (ICASSP). 2022; pp 3783–3787.
- (83) Tralie, C.; Saul, N.; Bar-On, R. Ripser.py: A Lean Persistent Homology Library for Python. *Journal of Open Source Software* **2018**, *3*, 925.
- (84) Rupp, M.; Tkatchenko, A.; Müller, K. R.; Lilienfeld, O. A. v. Fast and accurate modeling of molecular atomization energies with machine learning. *Physical Review Letters* **2012**, *108*.
- (85) De, S.; Bartók, A. P.; Csányi, G.; Ceriotti, M. Comparing molecules and solids across structural and alchemical space. *Phys. Chem. Chem. Phys.* **2016**, *18*, 13754–13769, Publisher: The Royal Society of Chemistry.
- (86) García-Andrade, X.; García Tahoce, P.; Pérez-Ríos, J.; Martínez Núñez, E. Barrier Height Prediction by Machine Learning Correction of Semiempirical Calculations. *J. Phys. Chem. A* **2023**, *127*, 2274–2283, Publisher: American Chemical Society.
- (87) Lundberg, S. M.; Lee, S.-I. A Unified Approach to Interpreting Model Predictions. Advances in Neural Information Processing Systems. 2017.
- (88) Hehre, W. J.; Ditchfield, R.; Stewart, R. F.; Pople, J. A. Self-Consistent Molecular Orbital Methods. IV. Use of Gaussian Expansions of Slater-Type Orbitals. Extension to Second-Row Molecules. *The Journal of Chemical Physics* **1970**, *52*, 2769–2773.
- (89) Parrish, R. M. et al. Psi4 1.1: An Open-Source Electronic Structure Program Emphasizing

Automation, Advanced Libraries, and Interoperability. *J. Chem. Theory Comput.* **2017**, *13*, 3185–3197, Publisher: American Chemical Society.

- (90) Smith, D. G. A. et al. Psi4NumPy: An Interactive Quantum Chemistry Programming Environment for Reference Implementations and Rapid Development. *J. Chem. Theory Comput.* **2018**, *14*, 3504–3511, Publisher: American Chemical Society.